Composites: Part A 188 (2025) 108516

Contents lists available at ScienceDirect

Composites Part A

journal homepage: www.elsevier.com/locate/compositesa

Freeform trajectory generation for fiber reinforced polymer composites additive manufacturing with variable-deposition-width

Danjie Bi [a,b], Pengcheng Hu [b], Zhaoyu Li [c], Jiancheng Hao [a], Kai Tang [a,b,d,*], Molong Duan [a,d,**]

[a] Department of Mechanical and Aerospace Engineering, Hong Kong University of Science and Technology, Hong Kong Special Administrative Region
[b] Smart Manufacturing Thrust, Hong Kong University of Science and Technology (Guangzhou), China
[c] School of Power and Mechanical Engineering, Wuhan University, China
[d] HKUST Shenzhen-Hong Kong Collaborative Innovation Research Institute, Futian, Shenzhen, China

ARTICLE INFO

Keywords:
Continuous carbon fiber-reinforced polymers
Trajectory generation
Streamline
Variable-deposition-width

ABSTRACT

Continuous carbon fiber-reinforced polymers (CCFRPs) printing is a unique additive manufacturing (AM) technique that enhances design flexibility and enables on-demand production of lightweight, high-strength composite parts. However, current trajectory generation methods for CCFRPs-AM have limited control over fiber placement and flexible matrix path infill, particularly in complex regions, often using constant deposition widths that restrict path coverage and mechanical properties. To address these limitations, this paper presents a variable-deposition-width (VDW) trajectory generation method for CCFRPs-AM. The approach integrates a streamline-based technique for fiber paths with a Voronoi diagram-based method for matrix path generation, optimizing path placement based on 2D stress fields while accommodating user-defined fiber paths. Mechanical tests by us on fabricated open-hole composite components demonstrate that the proposed approach enhances the interfacial bonding and increases the maximal loading capacity under tensile stress.

1. Introduction

Additive manufacturing (AM) has revolutionized the production of complex and customized components, offering great design flexibility. Among different AM techniques, the incorporation of carbon fiber-reinforced polymers (CFRPs) in AM stands out for its potential to produce high-strength, lightweight parts critical for advanced applications in aerospace, automotive, and healthcare fields [1]. CFRPs in CFRPs-AM are usually categorized into short carbon fiber-reinforced polymers and continuous carbon fiber-reinforced polymers (CCFRPs) [2]. Short fiber-reinforced polymers mix chopped fibers with polymer filaments before extrusion, which is easy-to-use and has enhanced properties but limited by the fiber length and fabrication defects [3]. By contrast, two main categories for CCFRPs-AM are “in-situ fusion” and “ex-situ prepreg” [4], which offers superior mechanical properties due to the continuous fibers' effective load transmission and structural integrity. This study employs an in-situ fusion CCFRPs-AM technique, where molten thermoplastic resin is mixed with continuous fibers, then extruded and consolidated under pressure.

In CCFRPs-AM, enhancing the strength and stiffness of CCFRP components while reducing weight remains the central objective among various approaches [5]. Strengths such as tensile, flexural, shear are influenced by processing parameters like layer thickness, temperature, and printing speed [6–8]. As investigated in [9–11], interfacial bonding between fibers and the matrix significantly impacts the composite mechanical properties, while the continuous fiber embedment reduces the risk of fiber pull-out. Path planning also significantly affects the reinforcement performance of fabricated CCFRP parts, wherein concentric and isotropic path infill patterns were commonly used [12–15]. However, the traditional path patterns are limited by the fixed fiber orientation, primarily due to the inadequate interfacial bonding, high porosity, and low fiber volume ratio [1]. Alternatively, aligning fibers catering to different loading conditions has the potential to enhance the strength, stiffness, or toughness [3]. The use of curvilinear fiber path, as introduced by Hyer et al. [16], improves the buckling resistance of composite components. Similarly, Vijayachandran et al. [17] utilized steered fiber paths for maximizing buckling loads considering control on unintended deviations that can cause gaps and overlaps. Besides, it is

* Corresponding author at: Smart Manufacturing Thrust, Hong Kong University of Science and Technology (Guangzhou), China.
** Corresponding author at: Department of Mechanical and Aerospace Engineering, Hong Kong University of Science and Technology, Hong Kong Special Administrative Region.
E-mail addresses: mektang@ust.hk (K. Tang), duan@ust.hk (M. Duan).

https://doi.org/10.1016/j.compositesa.2024.108516
Received 17 August 2024; Received in revised form 26 September 2024; Accepted 7 October 2024
Available online 18 October 2024
1359-835X/

also shown to minimize stress concentrations and reduce the compliance [18]. Boddeti et al. [19] generated paths parallel to maximal principal stress orientations to prevent shear failure in printed parts, thereby improving the mechanical performance. Other studies have aligned fiber orientations with stress lines [20–22], fluid streamlines [23], and force-flow paths [2,24], leveraging the anisotropic characteristics of fiber composites. However, these alignment methods can cause overlaps or gaps due to under-filling or over-filling in the printing region, when the width of the to-be-filled area differ from the nozzle diameter, increasing pressure within the extrusion system [25] and negatively affecting the mechanical performance [26].

Despite employing advanced feed control algorithms [27] or customized extrusion systems [28] to enhance deposition accuracy, the capability to dynamically control the printing width remains to be the key in path planning approaches to address the overlap or gap issues. Kuipers et al. [29] and Hornus et al. [30] employed a back pressure compensation method to vary the deposition width by adjusting the motion feed rate. This approach assumes a monotonic relationship between the back pressure exerted on the filament and deposition width, making it straightforward to implement. Xu et al. [31] proposed a stress-based path planning algorithm using grid discretization to adapt the path width to the toolpath orientation. However, limited path orientation choices from discretization restrain the adaptive path to only three specific directions. Unequal-width paths have been used to enhance deposition accuracy and efficiency in laser metal deposition and wire arc AM processes [32,33] but are usually limited to basic geometric shapes.

To address the aforementioned issues, this paper presents a novel trajectory generation approach that enables variable-deposition-width (VDW) CCFRPs-AM, combining a streamline-based method for fiber trajectories and a Voronoi diagram-based technique for matrix path generation. This approach allows control over fiber distribution according to the 2D stress field or a user-definition and adjusts deposition width in specific regions. Optimizing the fiber placement with VDW enhances interfacial bonding and load transfer, thereby improving the mechanical properties of the composite structure.

The workflow for the proposed VDW trajectory generation method is shown in Fig. 1, wherein the input allows for field traversed fiber paths or manually inputted freeform fiber paths. The subsequent sections of the paper are structured as follows: Section 2 introduces a novel VDW trajectory generation method for CCFRPs-AM. Section 3 presents detailed case studies and empirically validates the resultant simulations through fabrication and mechanical testing, demonstrating the approach's effectiveness. Finally, Section 4 provides the conclusions.

2. VDW trajectory generation

2.1. Streamline-based fiber path generation

The proposed VDW trajectory generation method aims to create coherent freeform printing trajectories defined by location and printing widths, effectively covering the entire enclosed region. This coverage is achieved by using fiber paths to enhance the mechanical strength and matrix paths to fill the spaces between the boundaries and existing fiber paths. The method accommodates various types of fiber paths, such as field-traversed streamlines or manually traced paths. In this section, a specific streamline-based fiber path generation method is adopted, which exploits the stress field to improve the mechanical performance.

Any freeform path of fiber encompasses three key factors: location, orientation, and deposition width. This section introduces location and orientation, while the deposition width distribution is covered in the next section. The procedure takes the enclosed polygonal region assigned with a 2D stress vector field as its input. Then, streamlines are extracted as fiber paths by tracing the field's flow, prioritizing generation in regions with high field magnitudes to those with low magnitudes. A streamline is defined as a tangential curve to the vector field at each point, and its construction consists of two main processes: seed placement and integration [34]. The seed placement selects the location of an initial point, known as a seed point. Originating from the seed point, the integration process iteratively elongates a streamline bi-directionally by resolving an ordinary differential equation over consecutive time intervals.

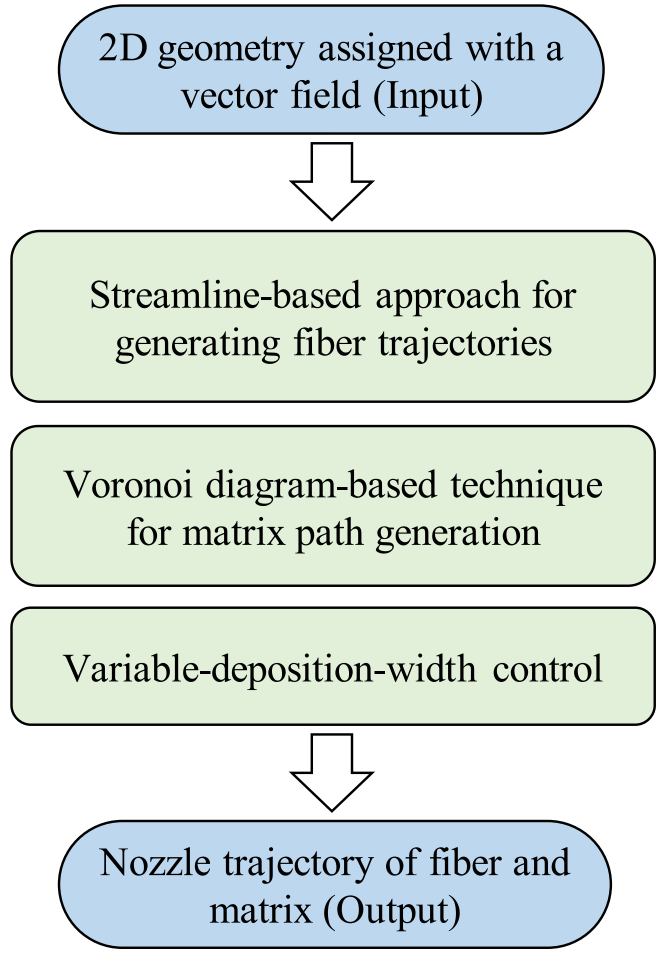

Fig. 1. Workflow for CCFRPs-AM path planning.

The core idea of the method is listed in Algorithm 1. The input consists of a 2D polygon domain numerically represented by a triangulated mesh $\mathscr{M}$ and a 2D stress field $\mathscr{T}$, assigned to the vertices $\mathscr{V}$ on $\mathscr{M}$. Two parameters Δl and d_{inf} respectively represent the step-size and influence distance in the integration process, while the output is the integrated streamlines. The algorithm begins with the seed point selection, which is selected from a seed pool consisting of all the candidate seeds positioned at the mesh vertices $\mathscr{V}$ by taking the one with the highest stress magnitude.

The first-order Euler numerical integration method is implemented from the seed point for streamlining construction. Letting p_k denote the current point position and p_{k+1} the next, the relation between the two can be written as follows:

$$p_{k+1} = p_k + \Delta l \frac{\vec{v}}{|\vec{v}|}, p_k \in \mathscr{V}, \tag{1}$$

where Δl denotes the integration step and $\vec{v}$ is the vector assigned at p_k in the stress field of the domain. The placement of the newly generated point p_{k+1} is not guaranteed to coincide with the mesh vertices. Therefore, the barycentric interpolation method is employed to determine the stress vector at p_{k+1} within the field. Through iterative integrations, a single streamline S_i is subsequently formed as a polyline, composed of a sequence of points, from the seed point in both the forward and backward directions with the specified step Δl. This process continues until the streamline either approaches another streamline or encounters the region boundary.

To generate streamlines with an appropriate density, we implement a new method to control the streamline distribution density by mitigating the stress magnitude around the generated streamline points among the field. Considering that the overall mechanical properties of the composite can be enhanced with fibers, the stress field undergoes updates after introducing the fiber paths (streamlines). Specifically, when a load is applied to the composite part, the fibers should bear a significant portion of it due to their high stiffness and strength. This effective load distribution minimizes stress concentrations and thus potential failure points. Consequently, the stress magnitude is mitigated around the generated streamlines by introducing a relaxation function. The relaxation function, denoted by $g(\bullet)$, is defined as a Gauss function representing the perturbation value at each vertex on the stress field $\mathscr{F}$ due to the introduction of streamline S_i. The function of $g(\bullet)$ varies with $d(\bullet)$, which is a function defining the Euclidean distance between the vertex $v \in \mathscr{V}$ and its nearest streamline point $p \in s$, which is mathematically expressed as

$$g(d(v,p)) = a\exp\left(-\frac{d(v,p)-b^2}{2c^2}\right), \tag{2}$$

where a, b and c are real constants based on the mean and standard deviation in a Gaussian distribution. By updating the field with the relaxation function, the updated expression for stress magnitude $|f_v|$ is described as follows:

$$|f_v'| = |f_v| - g(d(v,p)), f_v, f_v' \in \mathscr{F}. \tag{3}$$

On the other hand, practical streamline-placement prefers longer streamlines over shorter ones. Therefore, to elongate the nearby to-be-generated streamlines, the field within a specified range undergoes a further update by exerting an influence on its orientation along the constructed streamlines, aiming to maximize the directional consistency of adjacent streamlines. To realize this update, a so-called repulsion function is proposed to represent the perturbation in field direction as expressed in the following formula:

$$r\left(d(p_{s_m}, p_s)\right) = \mu\frac{m_1 m_2}{d(p_{s_m}, p_s)^2} = \mu\frac{|f_{s_m,v}||f_{s,v}|}{d(p_{s_m}, p_s)^2}, d(p_{s_m}, p_s) < \epsilon. \tag{4}$$

In Eq. (4), parameter μ denotes a constant that characterizes the perturbation degree. The variables of m_1 and m_2 correspondingly denote the stress magnitude at point $p_{S_m} \in S_m$ on an existing streamline and the current streamline point $p_s \in S_i$ within the stress field. To ensure effective operation of the repulsion force on vertices within a limited range, it is imperative to restrict the distance between p_{S_m} and p_s within a threshold ϵ. Thereby, the application of the repulsion function leads to the stress direction f_v, updated as follows:

$$\frac{f_v'}{|f_v'|} = \frac{f_v}{|f_v|} + r(d(p_{S_m}, p_S)). \tag{5}$$

Once the field is updated by the relaxation and repulsion functions (as outlined in Eq. (2)~(5)), the next iteration on seed point selection is influenced and the processed seed is also removed from the pool. Based on the aforementioned steps, the numerical integration method is iteratively applied to generate streamlines as fiber paths within the domain until the seed pool is exhausted.

Algorithm 1 streamlines generation within 2D stress field

Input: mesh $\mathscr{M}$, stress field $\mathscr{F}$, step size Δl, influence distance $d_{\inf}$

Output: streamlines S

```
/* initialization
ℛ ← initialize seeds pool as vertices of ℳ assigned with stress vector ℱ
n = 1
while seedsPool ≠ ∅ do
  seed ← CHOOSE SEED(ℛ, ℱ)
  /* Integration
  S_i ← STREAMLINE(seed, Δl, ℳ, ℱ), STREAMLINE(seed, −Δl, ℳ, ℱ)
/* Field update
  ℱ ← UPDATE_FIELD(d_inf, S, ℳ, ℱ); // Eq. (2)~(5)
  ℛ ← UPDATE_SEEDSPOOL(ℱ, ℛ);
  /* B-spline of streamlines
  S ← BSPLINE(S_i)
  n = n + 1
End
```

To achieve effective path coverage, the designated region is distinguished into a functional region and an auxiliary region. The functional region focuses on fiber paths catering to stress field orientation consistency, maximizing the coincidence of fiber orientation with the stress field orientation. The auxiliary region is designed to fill the fiber paths for path continuity. Correspondingly, distinct path patterns are implemented for the two types of regions. The functional region is specifically designed to accommodate streamlines, which enables the fiber orientation to align with the stress field to its maximum extent. By contrast, zigzag matrix paths are utilized to fill the auxiliary region, tailoring to printing continuity, as elaborated next.

2.2. Voronoi diagram-based matrix path generation

2.2.1. Fiber path neighborhood identification

Determining matrix paths in an enclosed 2D region with numerous fiber paths is complex due to the flexible and irregular nature of the fiber paths generated through various methods. To address this, we employ a generic matrix path generation approach using Voronoi diagrams, ensuring effective path coverage with VDW among the regions. A Voronoi diagram divides a 2D geometry into regions based on the proximity to a set of seed points, providing insights into the spatial distribution and relationships among these points. This makes it a powerful tool for subregion extraction within geometry, such as identifying neighboring zones among pre-determined fiber paths. In this study, the Voronoi diagram is constructed using the commonly employed Delaunay triangulation-based method.

To explain the generic approach of identifying neighboring zones through Voronoi diagrams, a simplified square geometry with a collection of curvilinear fiber paths is employed as a demonstrative example, as illustrated in Fig. 2(a). Given the 2D polygon domain G enclosed by a boundary B, a group of fiber paths are parametrized as B-formed splines and expressed as $S = \{S_1, S_2, \cdots, S_m\}$. Herein, $S_i(t_j)$ represents a specific path point of path S_i, and the spline parameterization variable t_j ranges from 0 to 1. All fiber path points S and discrete boundary points B are chosen as seed points for Voronoi diagrams construction and denoted as the set $D = S \cup B$, as exemplified in Fig. 2(a). Triangulating the seed points yields their Delaunay triangulation (Fig. 2(b)), whose dual graph produces the Voronoi diagram (Fig. 2(c)) of the seed points. In the Voronoi diagram, each seed point in D is assigned to the region associated with the nearest seed point, resulting in Voronoi cells, denoted as C. Additionally, the Voronoi vertices, represented by V, are determined as points equidistant between adjacent seed points, forming the intersections of the boundaries between adjacent cells. These boundaries, known as Voronoi edges, are defined by the perpendicular bisectors of lines connecting adjacent seeds and denoted by E.

For a sequence of seed points belonging to an arbitrary fiber path $S_i \in S$, a bunch of Voronoi cells that encompass S_i are extracted and marked as correlative cells of S_i. The left image of Fig. 2(d) shows the correlative region for the fiber path S_i, formed by combining these correlative cells and represented as $R(S_i)$. By tracing the Voronoi edges

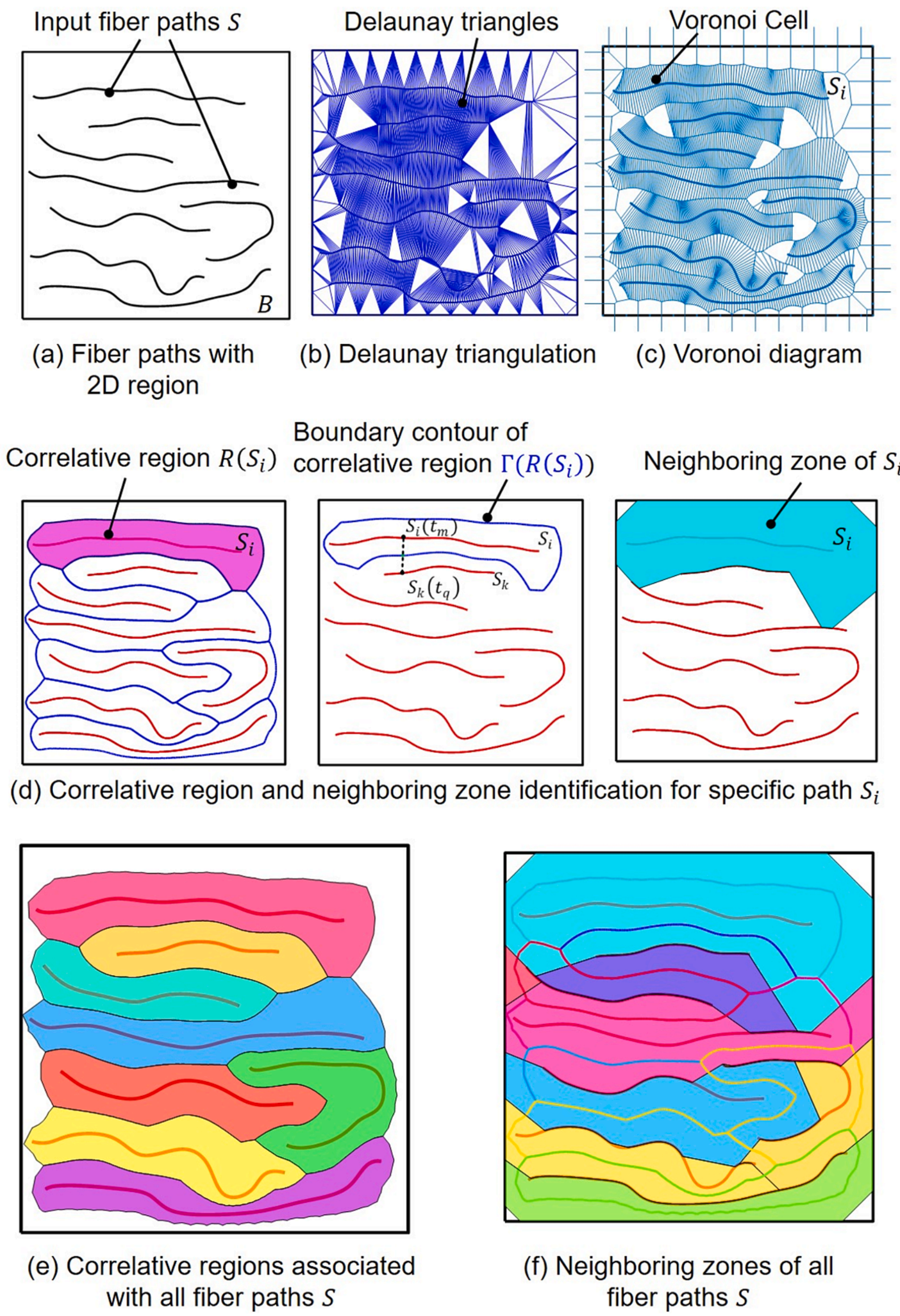

Fig. 2. Delaunay triangulation-based Voronoi diagram generation and neighboring zones identification.

of the enclosed region $R(S_i)$, an end-to-end boundary contour, regarded as $\Gamma(R(S_i))$, is obtained accordingly. The presence of $\Gamma(R(S_i))$ enables us to correlate seed points on S_i with other seeds located on either another fiber paths $S_j(j \neq i)$ or boundary B, as the Voronoi edge is a line segment that bisects two adjacent seed points. Accordingly, neighboring seed points of S_i can be derived by mirroring each seed in $S_i(t_m)$ with respect to the Voronoi edges in $\Gamma(R(S_i))$. This correlation establishes neighborhood relationships between seed points. As shown in the middle image of Fig. 2(d), the neighborhood of $S_i(t_m)$ specifically refers to $S_k(t_q)$, a path point on path S_k. Such neighborhood relations among such pair of points are termed as mutual neighbors, expressed as $S_i(t_m) \leftrightarrow S_k(t_q)$. Accordingly, for a path segment specified by $S_i(t_m, t_n)$ within interval $[t_m, t_n]$, its neighborhoods located on the same neighboring path are expressed as $S_k(t_q, t_w)$. The mirroring technique also effectively generates a neighboring zone around the fiber path S_i, as illustrated in the right image of Fig. 2(d). The neighboring zone, denoted as Z, is specifically defined as the region enclosed by a given fiber path segment and its neighborhood, where they share a mutual adjacency with one another and exhibit a direct connection to each other. Specifically, the neighboring zone for S_i and its neighboring denoted by $Z(S_i(t_m, t_n) \leftrightarrow S_k(t_q, t_w))$ is not intersected by any other neighboring zones, where the zone excludes the fiber or boundary itself.

With the established comprehensive neighborhood relationships, a consistent correspondence between the fiber paths and external boundaries is constructed within the confined region. Fig. 2 (e) and (f) illustrate the resultant correlative regions and neighboring zones, respectively, for all the fiber paths S. Each color block in the figure represents a distinct region/zone specific to its corresponding path. These neighboring zones are subsequently used to determine the variable path widths as detailed in the following section.

2.2.2. Variable-deposition-width optimization

The proposed matrix path generation method is accomplished through a two-step process. Firstly, the distribution of matrix width within the neighboring zone is determined by solving a constrained optimization problem, considering the known bounding path type and location. Secondly, by utilizing the optimized widths, the matrix points between fibers or the boundary are then generated through interpolation. Fig. 3 gives an explanation of matrix generation for a specific fiber path S_k within its neighboring zone (shown in blue) and the magnified view of this area is shown in Fig. 3(a). As illustrated in Fig. 3(b), the fiber path points on S_k within this zone $Z(S_k)$ are connected to their respective neighborhoods using the blue line segments. These line segments indicate where the matrix path points will be located, which will be further refined in subsequent steps. It is noted that each path point may have multiple neighbors, corresponding to segments of different neighbor paths without intersection.

Due to the practical printing requirements, changes in deposition width for both fiber and matrix paths are constrained within thresholds. Considering neighborhood relationships and width variation thresholds, the matrix path distribution problem is thus converted to minimizing the differences between the actual and the designed matrix-covered widths. To efficiently implement this one-off optimization of matrix widths, the maximum number of matrix points within zone $Z(S_k)$, denoted as $n_\mathrm{m}(S_k)$, are needed. To determine $n_\mathrm{m}(S_k)$, the matrix points number of any path point $S_k(t_k)$ on S_k, denoted by $n_\mathrm{m}(S_k(t_k))$, is calculated according to the following principles:

$$n_\mathrm{m}(S_k(t_k)) = \begin{cases} 0, & D_k < w_{\mathrm{m,min}} \\ 1, & D_k \in [w_{\mathrm{m,min}}, w_{\mathrm{m,max}}] \\ \lfloor D_k / w_{\mathrm{m,max}} \rfloor, & D_k > w_{\mathrm{m,max}},\ (D_k \bmod w_{\mathrm{m,max}}) < w_{\mathrm{m,min}} \\ \lfloor D_k / w_{\mathrm{m,max}} \rfloor + 1, & D_k > w_{\mathrm{m,min}},\ (D_k \bmod w_{\mathrm{m,max}}) \geqslant w_{\mathrm{m,min}} \end{cases}, \quad (6)$$

$$n_m(S_k) = \max\{n_\mathrm{m}(S_k(t_k))\}, S_k(t_k) \in S_k. \quad (7)$$

where D_k represents the gap distance between point $S_k(t_k)$ and its neighborhood. The minimum and maximum widths of the fiber path are denoted by $w_{\mathrm{f,min}}$, $w_{\mathrm{f,max}}$, respectively, while the corresponding denotations for the matrix path are $w_{\mathrm{m,min}}$ and $w_{\mathrm{m,max}}$.

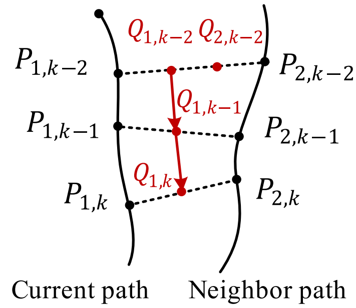

Fig. 4. Matrix point distribution between mutual neighboring paths.

Accordingly, the effective coverage of the designated gap distance within the neighboring zone facilitates the simultaneous optimization of deposition width for both the fiber and matrix components, given by:

$$\min\left\{\sum \left\| D_k - \left(\frac{W_1}{2} + \frac{W_2}{2} + \sum_i M_i\right) \right\| \right\}, i \in [0, n_m(S_k)], w_{\mathrm{f,min}} \le W_1, W_2 \le w_{\mathrm{f,max}}, w_{\mathrm{m,min}} \le M_i \le w_{\mathrm{m,max}}, \quad (8)$$

where W_1 and W_2 respectively represent the widths of the current fiber point and its neighborhood, and M_i expresses the matrix width distribution between mutual neighbor points. The neighbor patterns within a neighboring zone include the fiber–matrix and the fiber–fiber or fiber-boundary type. Considering the deposition width thresholds and the type of neighborhood (fiber or boundary), it is possible for W_1 or W_2 to become zero when the distance between the fiber and its neighborhoods is smaller than the deposition thresholds.

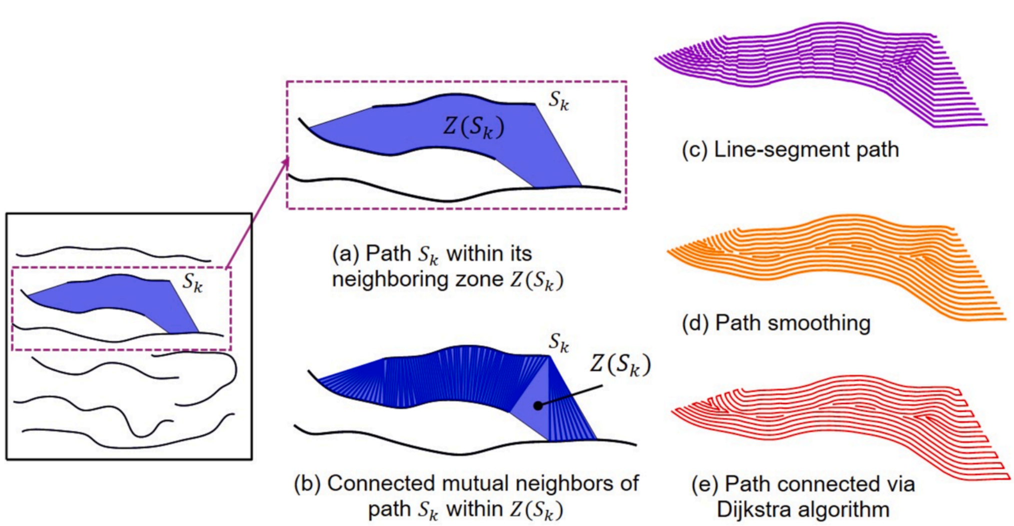

Fig. 3. Matrix path generation within a specific neighboring zone $Z(S_k)$.

Through optimization, the deposition width distributions of fiber widths, W_1 and W_2, and matrix widths $M_i(i \in [0, n_m(S_k))$ are quantitatively determined. However, the spatial distribution of matrix widths is not explicitly specified. A matrix filling order criterion is therefore introduced for specification: firstly, elements should be arranged in the descending order of width; secondly, placement near the fiber is prioritized, followed by that near the neighborhood of fiber. Then, as shown in Fig. 4, the matrix points $Q_{i,k}$ on S_k are localized through interpolation at the locations of line-segment endpoints, $P_{1,k}$ and $P_{2,k}$, as well as the matrix width distribution, as follows:

$$Q_{i,k} = (1-t)P_{1,k} + tP_{2,k}, \tag{9}$$

$$t = \frac{S_i}{D_k} = \frac{\sum_{n=1}^{i} X_k(n)}{D_k}, \ t \in [0,1], \tag{10}$$

$$X_k = [\frac{W_{1,k}}{2}, M_{1,k}, \cdots M_{i,k}, \cdots M_{n,k}, \frac{W_{2,k}}{2}]. \tag{11}$$

After applying the prescribed optimization and criteria, we generate the matrix paths by connecting consecutive matrix points, as demonstrated in Fig. 3(c). Subsequently, a post-processing procedure, based on smoothing the conformal mean curvature flow on curves, is employed to smooth the matrix paths within each neighboring zone, as depicted in Fig. 3(d). Furthermore, to enhance the printing efficiency, the Dijkstra algorithm is implemented to optimize the merging of neighboring matrix paths, as illustrated in Fig. 3(e).

2.3. VDW trajectory generator

Once the path locations and variable widths are determined, the material geometry modeling and quantitative representation of the motion become crucial for achieving the desired geometric accuracy in CCFRP fabrication. The matrix is comprised of a singular thermoplastic material, whereas the CCFRP comprises the fiber bundle and thermoplastic resin. In Fig. 5, the geometric modeling of the material extrusion process is depicted, illustrating how materials such as matrix, resin, and fibers are deposited through nozzles to construct composite structures. In Fig. 5 (a), the feed matrix material diameter for the matrix is denoted by d_m, while h and w denote the layer thickness and the deposited width, respectively. In Fig. 5(b), the material diameters for thermoplastic resin and fiber bundle are denoted by d_r and d_f respectively. The total volume of input is calculated by summing the cylinder volumes of input material in the following manner:

$$V_{1,m} = A_m L_m = \frac{\pi}{4} {d_m}^2 L_m,$$

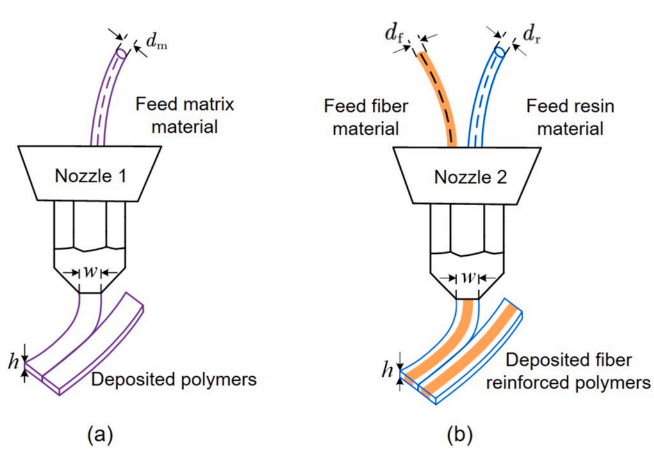

Fig. 5. Geometric modeling of the material extrusion process for (a) matrix and (b) fiber-reinforced polymer composites in CCFRPs-AM.

$$V_{1,c} = A_f L_f + A_r L_r = \frac{\pi}{4}\left({d_f}^2 L_f + {d_r}^2 L_r\right), \tag{12}$$

where $V_{1,m}$ and $V_{1,c}$ represent the input volume for matrix and composites, respectively. The symbol A_m, A_f, A_r denote the cross-sectional areas of matrix, fiber, and matrix, respectively; while L_m, L_f, L_r indicate the feed length of matrix, fiber, and resin material, respectively. The volume of the extruded material, denoted as V_2, is calculated based on the assumption of the cuboid model and expressed as follows:

$$V_2 = hwL_d, \tag{13}$$

where L_d denotes the deposited length after material solidification.

During fabrication, the material extruded from the nozzle matches the input amount ensuring volume equilibrium, which is mathematically expressed as $V_1 = \mu V_2$. The constant μ is related to material properties and the extrusion system, which can be determined through physical experiments. Accordingly, the printing width w for matrix and CCFRP can be deduced from Eq. (12)~(13) as follows:

$$w_m = \frac{\pi {d_m}^2 L_m}{4\mu_m h L_d},$$

$$w_c = \frac{\pi({d_f}^2 L_f + {d_r}^2 L_r)}{4\mu_c h L_d}. \tag{14}$$

Considering the material properties of fiber, the extruded CCFRP length is considered to be the same as the fiber feed distance, $L_d = L_f$, which physically means the ignorance of the tension of the fiber path during the printing. To simplify the above function, a factor δ is involved in expressing the ratio of resin and fiber feed length, written as $\delta = L_r/L_f$ with $\delta \in [0, 1]$.

$$w_c = \frac{\pi\left({d_f}^2 + {d_r}^2\delta\right)}{4\mu_c h}. \tag{15}$$

In the above function, d_f and d_r are material-specific parameters, whereas μ_c, μ_m and h are constant parameters once the materials and printing setup are determined. Thus, the variation of w can be expressed as a change in δ controlling the deposition width, while δ is constrained by the printing system limitations, such as the material properties and hardware configuration.

To achieve VDW printing, a back pressure compensation model constructed in [29] is adopted in this paper to correlate the feed rate $v(w)$ with the requested width w and layer thickness h in a linear form, as follows:

$$v(w) = \frac{f(w)}{hw}, \tag{16}$$

$$f(w) = f_r - k\left(\frac{w}{w_r} - 1\right). \tag{17}$$

The filament outflow, denoting the volumetric rate when the filament material is extruded, is intricately governed by the width w and is mathematically represented by $f(w)$. In Eq. (17), the compensation factor k adjusts the linear relationship, while f_r and w_r denote the constant reference flow and width, respectively. The reference flow f_r is derived from reference width w_r and feed v_r using $f_r = w_r v_r h$, where both parameters can be pre-tested through experiments.

As an example, Fig. 6 depicts the infill trajectory deposition width and motion speed corresponding to the geometry given in Fig. 3. The colors along the trajectory indicate the variations in widths and speeds, while the color bars provide a visual representation of the corresponding scalar values.

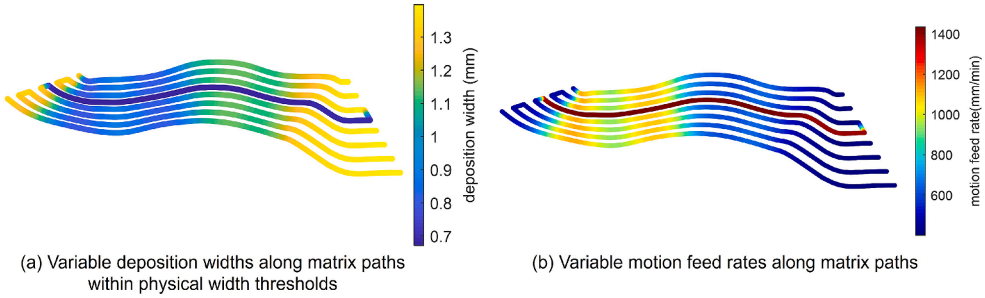

Fig. 6. Infill trajectory deposition width and motion speed corresponding to the geometry in Fig. 3.

Table 1
General invariable parameters of material and printing hardware.

Parameter	temperature (°C)	Nozzle diameter of plastics (mm)	Nozzle diameter of composites (mm)	Diameter of PLA (mm)	Diameter of carbon fiber (mm)
Value	210	0.4	0.8	1.75	0.34

3. Simulation and experimental results

3.1. VDW CCFRPs printing setup

An anisoprint Composite A4 printer configured with Bowden extrusion systems was adopted in this study for physical printing experiments, including the parametric design experiment and CCFRP parts fabrication. The printer was equipped with two nozzle print heads: one for the plastic matrix and another for continuous fiber with its respective resin material. Accordingly, polylactic acid (PLA) and impregnated carbon fiber composites, provided by the printer manufacturer, were employed for fabrication, where both the matrix and resin use PLA. Some basic invariable parameters of material and printing hardware used during the fabrication process are listed in Table 1. The material extrusion length of three types of materials were calculated following the formulas among Eq. (12)~(15), where $\mu_c, \mu_m = 1$ is adopted in this paper.

Based on the back pressure compensation model illustrated in Eq. (16)~(17), parameters k, f_r and w_r need to be identified practically for each printer system and material. A parametric design experiment, as depicted in Fig. 7, is thus designed to examine the impact of these parameters on the variability of deposition width along the trajectory. Fig. 7 illustrates a test region comprising stacked horizontal lines interconnected by perpendicular lines, where the print paths encompass four experimental groups. Each group consists of an experimental line and a corresponding stabilizer line, with the stabilizer line located above the experimental line to ensure the stability of internal pressure within the extrusion system during printing. Each experimental horizontal line comprises three distinct sections: sections A and C are situated at the beginning and end, respectively, while section B is positioned in the middle. Specifically, section B is printed to examine the dynamic response of the deposition width under varying printing parameters, such as feed rate and compensation factor, while other sections remain constant to ensure a steady printing condition.

In the compensation model mentioned in Eq. (17), the practical parameter k needs to be identified to achieve modeling construction. Due to the limited feed rate variation of CCFRP on the adopted composite printer, this study exclusively focused on controlling the deposition width variation in the matrix. The minimum and maximum width for matrix paths, $w_{m,min}$ and $w_{m,max}$, were set respectively as 0.6 mm and 1.4 mm, and the composite width w_c was set as 1 mm. As the compensation factor k influences the effect of feed rate on desired deposition widths, a group of parametric design experiments (as depicted in Fig. 7) were performed to determine a proper k for matrix paths. Under the current printing setup, Table 2 lists two groups of tests that provided the specific parameters employed. Factor k was first tested from 1 to 4 for rough evaluation; then a smaller range from 1 to 2.5 was further tested to identify a better value. Transiting from section A to section B, the desired deposition width was expected to vary from 1.4 mm to 0.6 mm before changing back to 1.4 mm when transiting to section C. With the given trajectory geometry as indicated in Fig. 7, a step increment of 0.2 mm was used to generate discrete path points, and motion feed rates along trajectories were calculated following Eq. (16)~(17).

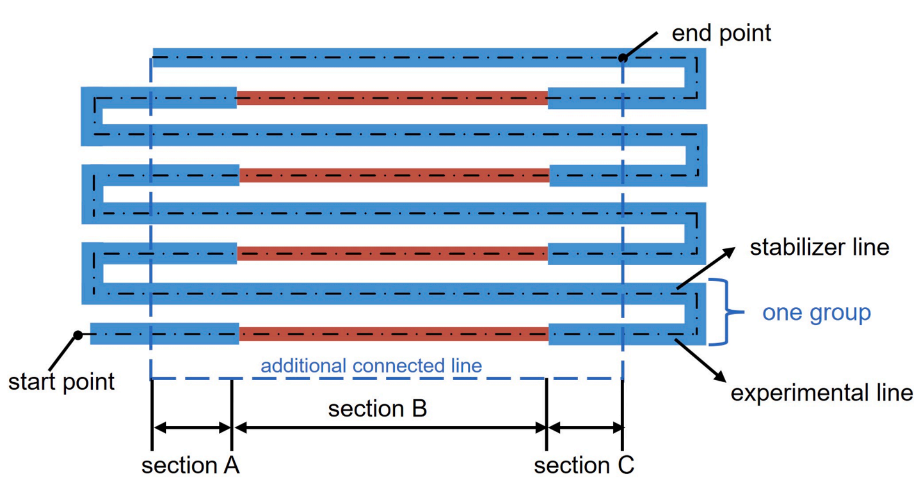

Fig. 7. Schematic of parametric design experiment.

Table 2
Parameters of parametric design.

Parameter	Undetermined factor k	Desired deposition width (mm)			Reference deposition width w_r (mm)	Reference feed rate v_r (mm/min)	Layer height h (mm)
		Section A	Section B	Section C			
Value	1, 2, 3, 4 1, 1.5, 2, 2.5	1.4	0.6	1.4	1	600	0.3

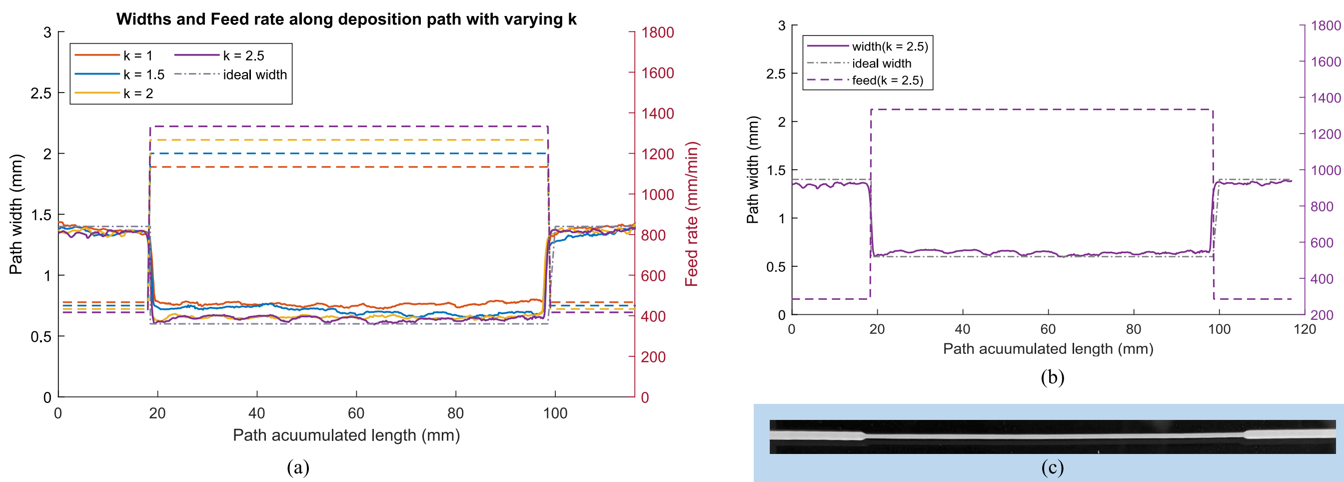

Fig. 8. Deposition widths and feed rate along trajectories with varying compensation factors.

To evaluate the difference between the actual and desired deposition width, an image processing technique from [35] was adopted to extract the actual deposition width from images captured after printing. The extracted actual deposition width and input feed rates along the deposition path for each (horizontal) experimental line in section A are shown in Fig. 8. The actual deposition width is represented by solid lines, while the input feed rates by dotted lines among different values of k. Evaluation of the results revealed that $k = 2.5$ yielded a satisfactory variation of the deposition width for our specific setup. The corresponding deposition width and feed rate for $k = 2.5$ were presented in Fig. 8(b), with widths ranging from 1.4 mm to 0.6 mm and feed rates varying from 416.7 mm/min to 1333.3 mm/min. On the other hand, Fig. 8(c) shows a higher printing speed in section B that led to a narrower deposition width, as compared to section A and C, due to the reduced material deposition time. Finally, the determined k was used to calculate the motion feed rate for printing the matrix in the ensuing VDW enabled printing experiment.

3.2. Case study on VDW trajectory generation

3.2.1. VDW trajectory generation of a looped-shape part

The printing process of CCFRP parts typically involves two types of deposition layers, where the continuous carbon fiber (CCF) layer consists of both fiber paths and matrix paths and the fused filament fabrication (FFF) layer only comprises matrix paths, serving to enhance the bonding between adjacent layers. To demonstrate the effectiveness of the proposed region-based fiber trajectory generation method, a commonly employed composite geometry, open-hole plate (shown in Fig. 9(a)), is adopted for case study. The selection of this model is motivated by its distinct shape, wherein the presence of the central hole in the plate results in reduced stiffness and strength, particularly under tensile or compressive loading conditions.

The CCF layer plays a critical role in improving the structural integrity and mechanical performance of the printed part. To optimize the CCF layer, the VWD trajectory generation method was implemented to reduce gaps and incomplete infill while considering the specific stress distribution within the part. Regarding the mesh represented 2D poly-

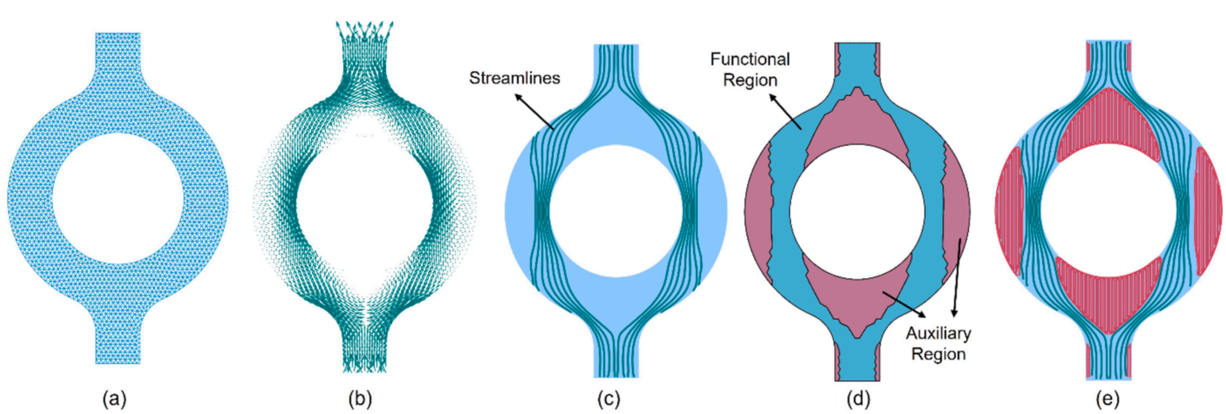

Fig. 9. Trajectory generation for 2D open-hole geometry: (a) triangulation; (b) coupled stress field σ_1; (c) streamlines traced from σ_1; (d) regional segmentation into the functional and auxiliary regions; and (e) matrix path infills within the auxiliary region.

gon domain (Fig. 9(a) paired with a specific stress field (Fig. 9(b))) as input, the procedure generates streamlines as fiber paths, aiming at aligning fiber orientations with the stress flow. Specifically, the stress field considered in this case is the maximal principal stress field resulting from the finite element analysis under uniaxial tension. The maximal principal stress, denoted as σ_1, represents the highest normal stress magnitude experienced at each vertex on the mesh, while its direction indicates the maximum potential for failure or yielding of structure. By implementing Algorithm 1, the streamlines were iteratively integrated within the provided stress field σ_1 resulting in the depicted results shown in Fig. 9(c). The streamlines, representing the fiber paths within the CCF layer, were deliberately designed to align with the stress distribution within the geometry, particularly in regions prone to stress concentration. This alignment enhances load transfer and reinforces the structural integrity of the printed component, thereby maximizing its strength and resistance to failure. With the streamlined fiber path generated, the functional region is subsequently formed by enclosing all the streamlines of appropriate lengths within the polygonal domain. By extracting the functional region from the original domain, a natural regional division is achieved, resulting in the formation of the auxiliary region as shown in Fig. 9(d). Since the auxiliary region consists of primarily matrix paths without any reinforcement, robust zigzag paths were applied to generate constant width infill paths for each sub-region within the auxiliary region, as depicted in dark red in Fig. 9(e).

In Fig. 9(e), paths in the auxiliary region are fully infilled with matrix paths, while the functional region consists of only fiber paths, leaving some space un-infilled. To ensure an optimized CCF layer with no incomplete infill, the proposed Voronoi diagram-based matrix path generation was implemented specifically for the functional region to generate appropriate matrix paths. The fiber trajectories within the functional region were generated as guided by the two stress fields tailored to the part's geometry, using the streamline-based approach as prescribed in Section 2.1. Specifically, two mutually orthogonal stress fields were respectively oriented along the maximal principal stress σ_1 and the minimal principal stress σ_3 fields. After the procedure given in Section 2.2, the resultant identified neighboring zones for two distinct conditions are presented in Fig. 10, where each color represents one specific neighboring zone for mutual neighbors. The resulting trajectories of fiber and matrix infill are presented in Fig. 11(b) and (c), with the fiber paths shown in red and matrix paths in pine green. In addition to the CCF layer, the FFF layer was infilled with zigzag matrix paths, as shown in Fig. 11(a). This augmentation serves to enhance the inter-layer

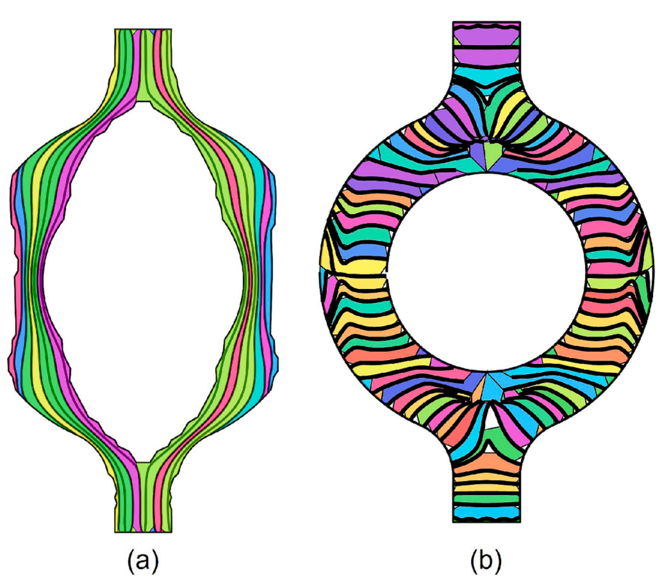

Fig. 10. Neighboring zone identification results for condition of (a) maximal principal stress field, and (b) minimal principal stress field extracted fiber paths.

bonding between CCF layers, thereby substantially improving the overall structural integrity of the fabricated objects. Finally, Fig. 11(d)&(e) show the depicted variable deposited paths, with (d) representing the paths generated from stress field σ_3, and (e) representing the paths generated from stress field σ_1.

To provide a comparative analysis, a conventional method for generating matrix paths based on given fiber paths was employed as a benchmark, whose corresponding process is illustrated in Fig. 12. Firstly, as shown in Fig. 12(a), a Boolean subtraction operation was performed on the 2D region. The specific regions corresponding to the fiber paths, along with their associated widths, are isolated and extracted from the original geometry. The remaining region after the Boolean subtraction, as depicted in Fig. 12(b), represents the specific area that requires filling with matrix paths. To generate matrix paths, the regions were divided into a bunch of sub-regions (Fig. 12(c)), in the form of polygons. After performing this division, zigzag paths along the longitudinal direction were generated which effectively filled all the sub-regions, as depicted in Fig. 12(d). The resulting pattern of paths was specifically designated as the reference group, serving as a basis for comparison in the subsequent analysis.

By integrating the CCF layer and FFF layer, the object exhibits a spatial distribution resembling a stack of CCF and FFF layers. As Fig. 13(a) depicted, a specific example illustrates a three-layer stacking distribution, with two FFF layers serving as the base before the printing of the single CCF layer. In scenarios involving multiple patterns of CCF layers, an unvarying single FFF layer is inserted between different CCF layers, with the CCF layer alternating within the spatial distribution, as Fig. 13(b) shows. To implement fabrication of CCFRP parts, the determined feed rate, the path location, and material extrusion lengths for a sequence of layers were encoded in G-code. Consequently, Fig. 13(c)-(f) showcase the resultant fabricated parts of the optimized group and reference group for two distinct configurations, respectively.

3.2.2. Experimental study of looped-shape part with VDW trajectory generation

In terms of tensile testing, the open-hole CCFRP specimens were tested to evaluate their mechanical behavior under uniaxial tension. The testing setup is shown in Fig. 14(a), where a universal tensile machine (UTM), Sintech 10/D from MTS was used, with the specimens securely fastened by both the upper and lower fixtures. During testing, specimens were subjected to a gradually increasing force at a 5 mm/min displacement rate until failure occurred, while the applied load and corresponding displacement were recorded. The mechanical testing procedure involved two configurations of open-hole specimens, each with an optimized and a reference group, totaling four fabricated CCFRP specimens. In the first configuration, the paths within the CCF layer were generated solely based on the maximal principal stress field σ_1, while in the second configuration, the CCF layer incorporated fiber paths generated alternately from either the maximal or minimal principal stress fields (σ_1 or σ_3). The resultant load–displacement curves from these two configurations are respectively presented in Fig. 14(b) and Fig. 14(c).

The first configuration as shown in Fig. 14(b) revealed that the maximal load did not significantly differ between the optimized group and the reference group. This can be attributed to the high similarity in the matrix paths generated by both groups. As demonstrated in Fig. 11(c) and Fig. 12(d), the fiber paths of the optimized group, obtained from σ_1 field, resulted in curvilinear matrix paths approximately along the longitudinal direction. Similarly, the reference group also produced longitudinal linear-parallel (zigzag) matrix paths, thereby leading to both groups exerting a comparable influence on the load-bearing capacity of the specimens under the given condition. By contrast, for second configuration shown in Fig. 14(c), a 19 % increase in the maximal loading capacity of the specimens was achieved, rising from 1291.8 N (reference group) to 1537.5 N (optimized group). This indicates that the VDW-optimized group, with alternating fiber paths

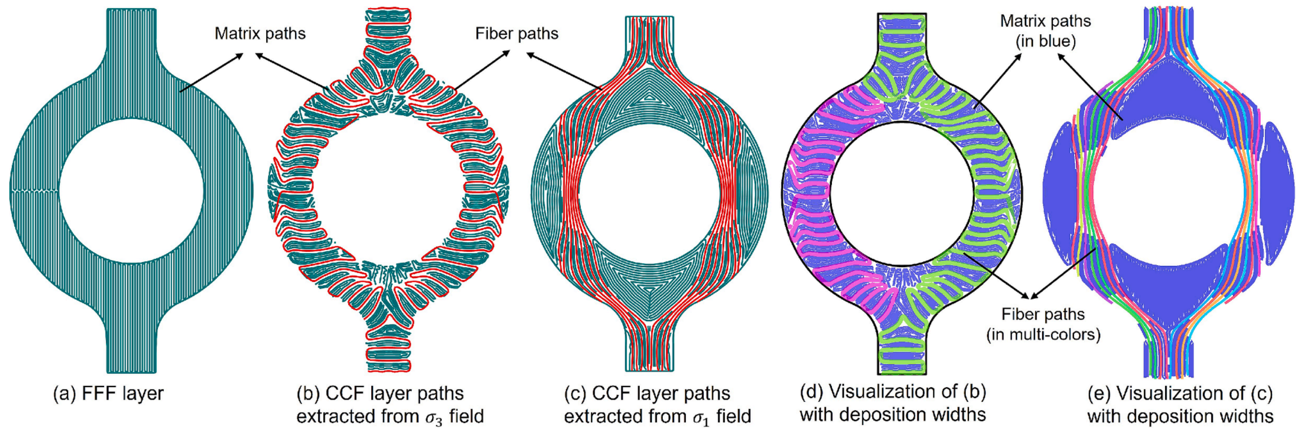

Fig. 11. Printing trajectories of FFF and CCF layers.

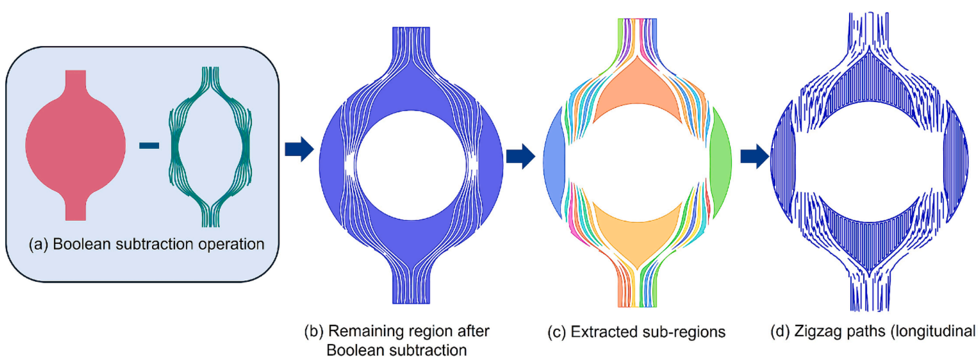

Fig. 12. Path generation steps for the reference group: (a) Boolean subtraction of the original model by equal width fibers; (b) the remaining regions after the Boolean subtraction; (c) the extracted sub-regions; and (c) the zigzag paths generated for all the sub-regions.

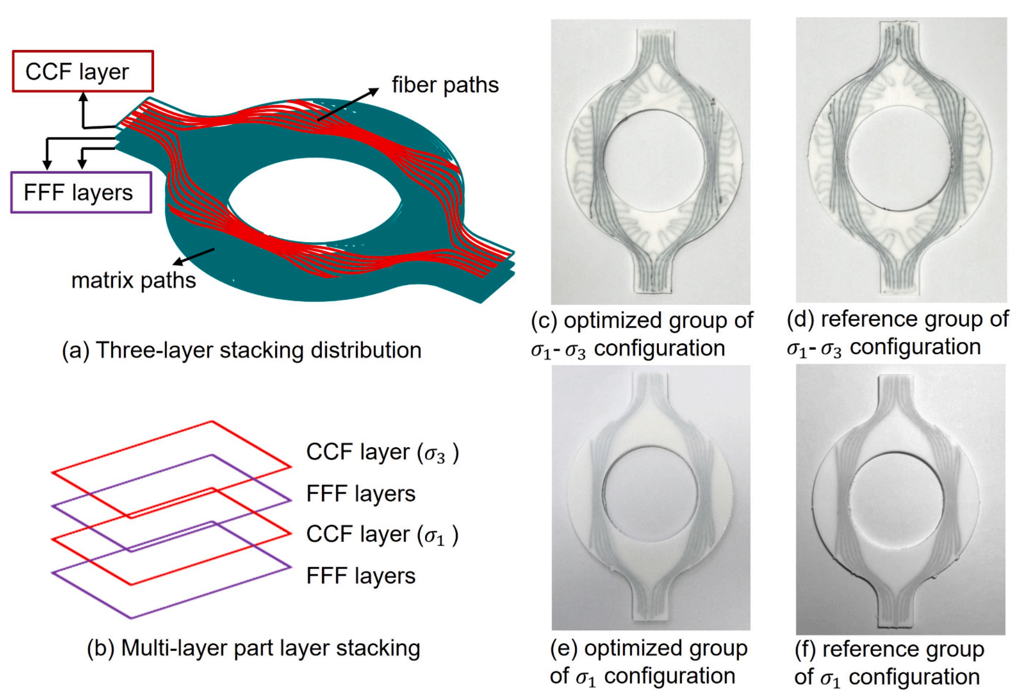

Fig. 13. Spatial distribution of printing layers, and the fabricated parts of the optimized group and reference group.

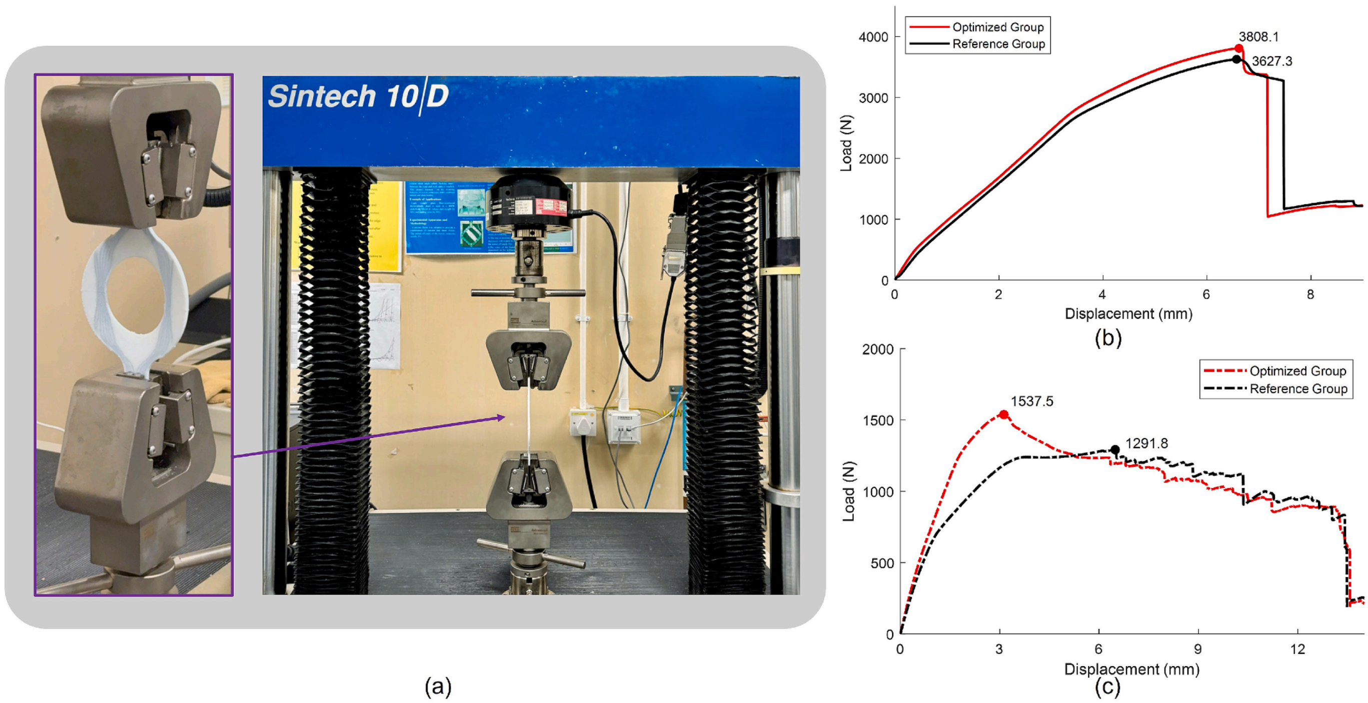

Fig. 14. (a) Tensile testing setup using a UTM and load-extension curves comparing the optimized group and reference group under (b) the first configuration utilizing σ_1, and (c) the second configuration utilizing both σ_1 and σ_3 for the open-hole specimen.

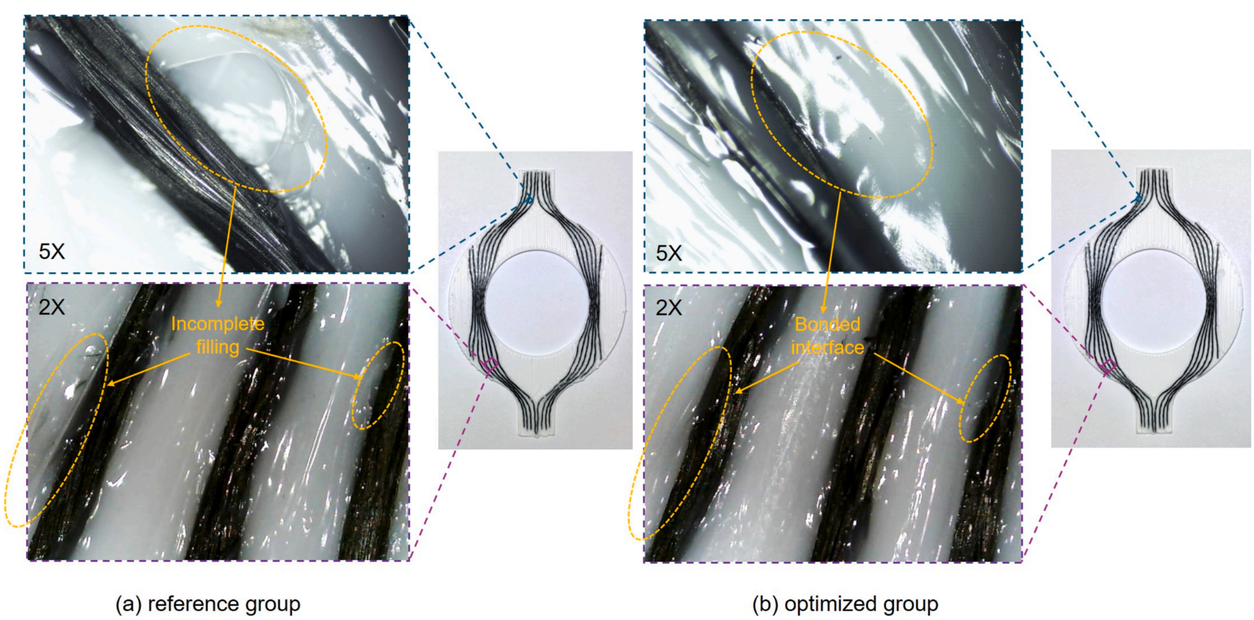

Fig. 15. Surface characteristics of the fabricated open-hole specimen for (a) the reference group and (b) the optimized group under a digital microscope.

between σ_1 and σ_3 stress field, achieved superior enhancement compared to the reference group. The gradual decrease in load suggests great energy absorption and ductile behavior of the CCFRP components. The stress field σ_1 induced fiber alignments enhanced the mechanical properties by ensuring fibers to align with the loading direction, effectively transmitting the force and maximizing the tensile resistance. On the other hand, the lower load-bearing capacity (Fig. 14(c)) as compared to the first configuration (Fig. 14(b)) is also obviously noticed, which is chiefly due to the orthogonal relationship between the σ_3 field induced fiber paths and the loading direction which potentially weakens the CCFRP components and increases the risk of failure along the fiber–matrix interfaces.

Surface characteristics were examined within the CCF layer using a Ken-A-Vision Kena digital microscope. For convenient observation, three-layered specimens were fabricated, consisting of two base FFF layers and one CCF layer on the top. Under the microscope, the surface characteristics of the specimens, specifically the interface bonding condition between the fiber and matrix paths, were thoroughly observed. To conduct a better direct comparison between the optimized and the reference groups, both groups were examined at the same location. In Fig. 15, representative locations are highlighted using solid colored boxes, and larger views for visual observation of bonding quality are provided in dashed-colored rectangles for both groups. The labels of 2X and 5X denote the magnification of the microscope for captured images, respectively. As Fig. 15(a) indicates, the reference group displayed inadequate filling between the fiber and matrix paths, marked by yellow ellipses, suggesting potential weakness in the interface bonding. Such defect acts as a structural defect and is typically responsible for prospective structural failure of fabricated parts. Though void formation is an inherent limitation of additive manufacturing, it can be mitigated through advanced path planning and optimization of processing parameters. Fig. 15 (b) presents the surface characteristics of the printed parts using the proposed optimized approach. The image revealed a complete bonded interface between the components (at the circled location), with a more uniform and smooth surface texture in the optimized group compared to the reference group (Fig. 15(a)). This improvement can be attributed to the adoption of the VDW approach, which allows for adaptation to the varying spaces between the fiber paths, minimizing gaps and inadequate infill. The visualization highlights the positive effects of the optimized approach on the surface characteristics and overall quality of the printed components, thereby further supporting the potential benefits of the proposed approach in improving maximal loading capacity under the tensile stress of CCFRP objects.

4. Conclusion

In this study, we present a VDW-enabled trajectory generation method for CCFRP printing that integrates a streamline-based algorithm for fiber trajectories with a Voronoi diagram-based technique for matrix path generation. This method aims to reduce gaps between fiber and matrix paths and enhance interfacial bonding and load transfer by controlling fiber and matrix path placements with variable deposition widths. Using an open-hole geometry as an illustrative example, the streamline-based algorithm allows dynamic control of fiber distribution based on the 2D stress field, such as the maximal principal stress field associated with the geometry, to guide the fiber path placement. Notably, the proposed method is not limited to field-traversed fiber paths, as it is also adaptable to manually defined freeform fiber paths. With the fiber path determined, a Voronoi diagram-based matrix path generation method is then presented that enables us to plan the matrix path placement and optimize variable deposition widths for both the fiber and matrix paths.

In the experiments, accompanied by the utilization of a compensation model to adjust the feed rate, printing parameters with variable width deposition control were identified for fabrication, which used a continuous fiber 3D printer to produce CCFRP specimens. The tensile testing and surface characterization were conducted on fabricated CCFRP specimens through a comparative analysis between the proposed method and reference groups. Through examination of the test results, it is found that incomplete infills between the fiber and matrix paths were diminished when adapting the deposition width based on the regional characteristics, leading to enhanced bonding between adjacent paths. Consequently, the proposed approach helps enhance the load transfer efficiency and mitigates the risk of delamination, leading to improved mechanical properties of CCFRP parts. However, we acknowledge that the current method offers limited evaluation of surface characteristics. Future studies may use quantitative indices, such as porosity in fabricated specimens, as assessment indicators for path planning optimization, thus, to enhance the comprehensiveness of evaluation. In conclusion, the findings of this research provide insights into the implementation of VWD-enabled trajectory generation techniques for CCFRPs-AM, opening up new opportunities for optimizing the manufacturing process and achieving superior performance in fiber-reinforced composite applications.

CRediT authorship contribution statement

Danjie Bi: Writing – original draft, Validation, Methodology, Conceptualization. **Pengcheng Hu:** Supervision. **Zhaoyu Li:** Writing – review & editing. **Jiancheng Hao:** Validation. **Kai Tang:** Writing – review & editing, Supervision, Project administration. **Molong Duan:** Writing – review & editing, Supervision, Methodology, Conceptualization.

Declaration of competing interest

The authors declare that they have no known competing financial interests or personal relationships that could have appeared to influence the work reported in this paper.

Data availability

No data was used for the research described in the article.

Acknowledgements

The authors acknowledge support from the Research Grants Council (RGC) of the Government of Hong Kong Special Administrative Region (HKSAR) with RGC/ECS Project (No. 26215824), and HKUST Bridge Gap Fund (BGF). This work was supported in part by the Project of Hetao Shenzhen-Hong Kong Science and Technology Innovation Cooperation Zone (HZQB-KCZYB-2020083) and the Guangzhou-HKUST(GZ) Joint Funding Program (No. 2024A03J0680).

References

[1] Dey A, Eagle INR, Yodo N. A review on filament materials for fused filament fabrication. J Manuf Mater Process 2021;5(3). https://doi.org/10.3390/jmmp5030069.
[2] Li S, Xin Y, Yu Y, Wang Y. Design for additive manufacturing from a force-flow perspective. Mater Des 2021;204:109664. https://doi.org/10.1016/j.matdes.2021.109664.
[3] van de Werken N, Tekinalp H, Khanbolouki P, Ozcan S, Williams A, Tehrani M. Additively manufactured carbon fiber-reinforced composites: state of the art and perspective. Addit Manuf 2020;31:100962. https://doi.org/10.1016/J.ADDMA.2019.100962.
[4] Goh GD, Dikshit V, Nagalingam AP, Goh GL, Agarwala S, Sing SL, et al. Characterization of mechanical properties and fracture mode of additively manufactured carbon fiber and glass fiber reinforced thermoplastics. Mater Des 2018;137:79–89. https://doi.org/10.1016/J.MATDES.2017.10.021.
[5] Sugiyama K, Matsuzaki R, Malakhov AV, Polilov AN, Ueda M, Todoroki A, et al. 3D Printing of optimized composites with variable fiber volume fraction and stiffness using continuous fiber. Compos Sci Technol 2020;186:107905. https://doi.org/10.1016/J.COMPSCITECH.2019.107905.
[6] Li N, Li Y, Liu S. Rapid prototyping of continuous carbon fiber reinforced polylactic acid composites by 3D printing. J Mater Process Technol 2016;238:218–25. https://doi.org/10.1016/J.JMATPROTEC.2016.07.025.
[7] Justo J, Távara L, García-Guzmán L, París F. 2018, "Characterization of 3D Printed Long Fibre Reinforced Composites". Compos Struct October 2017;185:537–48. https://doi.org/10.1016/j.compstruct.2017.11.052.
[8] Yu T, Zhang Z, Song S, Bai Y, Wu D. Tensile and flexural behaviors of additively manufactured continuous carbon fiber-reinforced polymer composites. Compos Struct 2019;225(April):111147. https://doi.org/10.1016/j.compstruct.2019.111147.
[9] Caminero MA, Chacón JM, García-Moreno I, Reverte JM. Interlaminar bonding performance of 3D printed continuous fibre reinforced thermoplastic composites using fused deposition modelling. Polym Test 2018;68:415–23. https://doi.org/10.1016/J.POLYMERTESTING.2018.04.038.
[10] Dickson AN, Barry JN, McDonnell KA, Dowling DP. Fabrication of continuous carbon, glass and Kevlar fibre reinforced polymer composites using additive manufacturing. Addit Manuf 2017;16:146–52. https://doi.org/10.1016/J.ADDMA.2017.06.004.
[11] Jahangir MN, Billah KMM, Lin Y, Roberson DA, Wicker RB, Espalin D. Reinforcement of material extrusion 3D printed polycarbonate using continuous carbon fiber. Addit Manuf 2019;28:354–64. https://doi.org/10.1016/J.ADDMA.2019.05.019.
[12] Baumann F, Scholz J, Fleischer J. Investigation of a new approach for additively manufactured continuous fiber-reinforced polymers. Procedia CIRP 2017;66:323–8. https://doi.org/10.1016/j.procir.2017.03.276.
[13] Tian X, Liu T, Yang C, Wang Q, Li D. Interface and performance of 3D printed continuous carbon fiber reinforced PLA composites. Compos Part A Appl Sci Manuf 2016;88:198–205. https://doi.org/10.1016/J.COMPOSITESA.2016.05.032.

[14] Matsuzaki R, Ueda M, Namiki M, Jeong TK, Asahara H, Horiguchi K, et al. Three-dimensional printing of continuous-fiber composites by in-nozzle impregnation. Sci Rep 2016;6. https://doi.org/10.1038/srep23058.
[15] Araya-Calvo M, López-Gómez I, Chamberlain-Simon N, León-Salazar JL, Guillén-Girón T, Corrales-Cordero JS, et al. Evaluation of compressive and flexural properties of continuous fiber fabrication additive manufacturing technology. Addit Manuf 2018;22:157–64. https://doi.org/10.1016/J.ADDMA.2018.05.007.
[16] Hyer MW, Lee HH. The use of curvilinear fiber format to improve buckling resistance of composite plates with central circular holes. Compos Struct 1991;18(3):239–61. https://doi.org/10.1016/0263-8223(91)90035-W.
[17] Vijayachandran AA, Davidson P, Waas AM. Optimal fiber paths for robotically manufactured composite structural panels. Int J Non Linear Mech 2020;126. https://doi.org/10.1016/J.IJNONLINMEC.2020.103567.
[18] Shafighfard T, Demir E, Yildiz M. Design of fiber-reinforced variable-stiffness composites for different open-hole geometries with fiber continuity and curvature constraints. Compos Struct 2019;226(August):1–14. https://doi.org/10.1016/j.compstruct.2019.111280.
[19] Boddeti N, Tang Y, Maute K, Rosen DW, Dunn ML. Optimal design and manufacture of variable stiffness laminated continuous fiber reinforced composites. Sci Rep 2020. https://doi.org/10.1038/s41598-020-73333-4.
[20] Tam KMM, Mueller CT. Additive manufacturing along principal stress lines. 3D Print Addit Manuf 2017;4(2):63–81. https://doi.org/10.1089/3dp.2017.0001.
[21] Zhang H, Li A, Wu J, Sun B, Wang C, Yang D. Effectiveness of fibre placement in 3D printed open-hole composites under uniaxial tension. Compos Sci Technol 2022;220. https://doi.org/10.1016/J.COMPSCITECH.2022.109269.
[22] Malakhov AV, Tian X, Zheng Z, Plugatar TP, Huang Y, Tatus NA, et al. Three-dimensional printing of biomimetic variable stiffness composites with controlled orientations and volume fraction of fibers. Compos Struct 2022;299(June):116091. https://doi.org/10.1016/j.compstruct.2022.116091.
[23] Khan S, Fayazbakhsh K, Fawaz Z, Arian Nik M. Curvilinear variable stiffness 3D printing technology for improved open-hole tensile strength. Addit Manuf 2018;24(June):378–85. https://doi.org/10.1016/j.addma.2018.10.013.
[24] Wang T, Li N, Link G, Jelonnek J, Fleischer J, Dittus J, et al. Load-dependent path planning method for 3D printing of continuous fiber reinforced plastics. Compos Part A Appl Sci Manuf 2021;140:106181. https://doi.org/10.1016/J.COMPOSITESA.2020.106181.
[25] Kabir SMF, Mathur K, Seyam AFM. A critical review on 3D printed continuous fiber-reinforced composites: history, mechanism, materials and properties. Compos Struct 2020;232. https://doi.org/10.1016/J.COMPSTRUCT.2019.111476.
[26] Xia L, Lin S, Ma G. 2020, "Stress-Based Tool-Path Planning Methodology for Fused Filament Fabrication". Addit Manuf September 2019;32:101020. https://doi.org/10.1016/j.addma.2019.101020.
[27] Wu P, Ramani KS, Okwudire CE. Accurate linear and nonlinear model-based feedforward deposition control for material extrusion additive manufacturing. Addit Manuf 2021;48(PB):102389. https://doi.org/10.1016/j.addma.2021.102389.
[28] Gharehpapagh B, Dilberoglu UM, Yaman U, Dolen M. Adaptive toolpath generation for material extrusion additive manufacturing using a nozzle with rectangular orifice. Addit Manuf 2023;78:103873. https://doi.org/10.1016/J.ADDMA.2023.103873.
[29] Kuipers T, Doubrovski EL, Wu J, Wang CCL. A framework for adaptive width control of dense contour-parallel toolpaths in fused deposition modeling. CAD Computer Aided Design 2020;128:102907. https://doi.org/10.1016/j.cad.2020.102907.
[30] Hornus S, Kuipers T, Devillers O, Teillaud M, Martínez J, Glisse M, et al. Variable-width contouring for additive manufacturing. ACM Trans Graph 2020.
[31] Xu W, Xu H, Li Q, Zhang P, Yang L, Wang W. Stress-based continuous planar path planning for additive manufacturing. Adv Eng Softw 2024;188:103544. https://doi.org/10.1016/J.ADVENGSOFT.2023.103544.
[32] Shi T, Lu B, Shen T, Zhang R, Shi S, Fu G. Closed-loop control of variable width deposition in laser metal deposition. Int J Adv Manuf Technol 2018;97(9–12):4167–78. https://doi.org/10.1007/s00170-018-1895-z.
[33] Xiong Y, Park SI, Padmanathan S, Dharmawan AG, Foong S, Rosen DW, et al. Process planning for adaptive contour parallel toolpath in additive manufacturing with variable bead width. Int J Adv Manuf Technol 2019;105(10):4159–70. https://doi.org/10.1007/s00170-019-03954-1.
[34] Mebarki A, Alliezy P, Devillers O. Farthest point seeding for efficient placement of streamlines. IEEE Visualization 2005:479–86. https://doi.org/10.1109/visual.2005.1532832.
[35] Chen S, Yang Y, Liu S, Duan M. In-situ additive manufacturing deposition trajectory monitoring and compensation with thermal camera. Addit Manuf 2023;78:1–25. https://doi.org/10.1016/j.addma.2023.103820.